Chinese Chemical Letters 36 (2025) 110088

Contents lists available at ScienceDirect

Chinese Chemical Letters

journal homepage: www.elsevier.com/locate/cclet

Robust assembly of TiO_2 quantum dots onto $Ti_3C_2T_x$ for excellent lithium storage capability

Xinlin Zhang[a], Cheng Tang[b], Haitao Li[a], Jie Sun[a], Aijun Du[b], Minghong Wu[a], Haijiao Zhang[a,c,*]

[a] Institute of Nanochemistry and Nanobiology, School of Environmental and Chemical Engineering, Shanghai University, Shanghai 200444, China
[b] School of Chemistry and Physics and Centre for Materials Science, Queensland University of Technology, Brisbane, QLD 4001, Australia
[c] Key Laboratory of Advanced Energy Materials Chemistry (Ministry of Education), Nankai University, Tianjin 300071, China

ARTICLE INFO

Article history:
Received 21 May 2024
Accepted 4 June 2024
Available online 4 June 2024

Keywords:
TiO_2 quantum dots
$Ti_3C_2T_x$ MXene
Robust assembly
Lithium-ion batteries
Anode materials

ABSTRACT

TiO_2 has been widely studied as one of the most promising anode materials for lithium-ion batteries (LIBs) due to good structural stability and small volume changes. However, its applications are still greatly affected by its poor electrical conductivity. In this work, ultrasmall TiO_2 quantum dots (QDs) are firmly grown onto 2D $Ti_3C_2T_x$ nanosheets (A-TiO_2/$Ti_3C_2T_x$), benefiting from the positive regulation of (3-aminopropyl)triethoxysilane (APTES). Interestingly, SiO_2 nanoparticles produced by the hydrolysis of APTES can strengthen the strong coupling of TiO_2 QDs with $Ti_3C_2T_x$, thereby enhancing the structural integrity of the composite. As expected, the A-TiO_2/$Ti_3C_2T_x$ composite demonstrates an exceptional lithium storage performance, achieving a high capacity of 425.4 mAh/g for 400 cycles at 0.1 A/g, and an outstanding long-term cycling stability. *In-situ* electrochemical impedance spectroscopy and theoretical analysis unconver that the superior lithium storage performance is attributed to its unique heterostructure and *in-situ* N doping derived from APTES, which not only reduces the Li^+ adsorption energy, but also gives the fast charge transfer dynamics.

To date, lithium-ion batteries (LIBs) stand out as one of the most dependable and practical devices owing to their high energy/power density and eco-friendliness [1]. However, the graphite anode utilized by LIBs suffers from low capacity, which brings new challenges in meeting the increasing demand for high-performance energy storage in rapidly evolving electronic devices [2]. Therefore, it is necessary to further develop high-performance LIBs anode materials with high capacity and long cycling life.

Of these anode materials, titanium dioxide (TiO_2) has been regarded as a promising anode material for LIBs, owing to its good structural stability and small volume changes (~5%) [3], in contrast to other metal oxides such as Nb_2O_5 [4], and MoO_3 [5]. These features can effectually improve the cycling stability of the TiO_2 electrode and prolong its operational lifespan. However, its inherent low conductivity and slow electrochemical reaction kinetics remain obstacles for achieving the high lithium storage performance. To address these issues, various approaches have been developed. For example, nanostructured engineering of TiO_2 materials is one of the most effective strategies. To date, nanosheet [6,7], nanowire [3], and nanotube [8] structured TiO_2 have been successfully prepared, demonstrating an improved electrochemical performance [9]. On the other hand, the conductivity of TiO_2 can be markedly enhanced by combining it with some two-dimensional (2D) conductive matrix. Specifically, $Ti_3C_2T_x$ MXene exhibits distinct advantages in lithium-ion storage owing to exceptional conductivity and unique 2D structure [10,11]. Consequently, incorporating TiO_2 nanoparticles onto $Ti_3C_2T_x$ holds significant promise for boosting their lithium storage performance. For instance, Shakoor *et al.* [12] loaded TiO_2 particles onto the $Ti_3C_2T_x$ surface, resulting in a specific discharge capacity of 200 mAh/g at 0.1 C. Additionally, Li *et al.* [13] prepared the Ti_3C_2@TiO_2 MXene hybrid and exhibited a capacity of 302 mAh/g after 500 cycles at 200 mA/g. Nevertheless, the obtained TiO_2 particles generally have large size and unstable combination between TiO_2 and $Ti_3C_2T_x$, leading to the dissatisfactory electrochemical performance. As a unique nanostructure, zero-dimensional (0D) quantum dots (QDs) have garnered growing attention in LIBs due to their maximized surface area exposure and minimized charge diffusion distance [14,15]. More importantly, QDs can effectively buffer large volume expansion during ion inser-

* Corresponding author at: Institute of Nanochemistry and Nanobiology, School of Environmental and Chemical Engineering, Shanghai University, Shanghai 200444, China.
E-mail address: hjzhang128@shu.edu.cn (H. Zhang).

https://doi.org/10.1016/j.cclet.2024.110088
1001-8417/

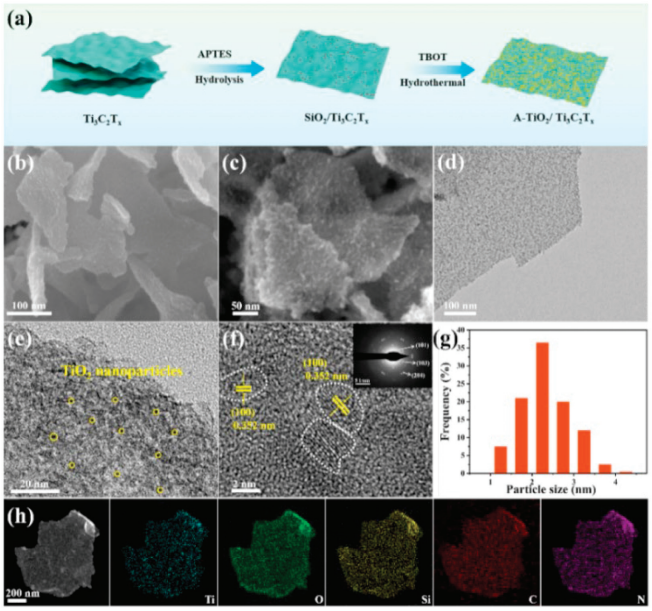

Fig. 1. (a) The fabrication process of A-$TiO_2/Ti_3C_2T_x$. (b, c) SEM images, (d) TEM image, (e, f) HRTEM images (insert is the SAED pattern), (g) particle size distribution profile, and (h) STEM image and corresponding elemental mappings of A-$TiO_2/Ti_3C_2T_x$.

tion/extraction. Besides, the SiO_2 with excellent rigidity has been demonstrated to be an effective stabilizer for the composite materials in previous study [16]. Therefore, exploring the facile method for robust assembly of TiO_2 QDs onto $Ti_3C_2T_x$ nanosheets by the incorporation of SiO_2 particles is anticipated to significantly enhance the lithium storage performance of the composite, especially its cycling stability.

In this work, we design a new 0D/2D heterostructure (namely, A-$TiO_2/Ti_3C_2T_x$) through a scalable hydrothermal process induced by (3-aminopropyl)triethoxysilane (APTES). The results indicate that the SiO_2 nanoparticles produced by the hydrolysis of APTES contribute to a strong coupling effect between TiO_2 QDs and $Ti_3C_2T_x$ nanosheets. Such a unique configuration endows the A-$TiO_2/Ti_3C_2T_x$ anode with an extremely high capacity and long-term cycling life for lithium storage. Furthermore, *in-situ* electrochemical impedance spectroscopy (EIS) indicates that the remarkable structural stability of A-$TiO_2/Ti_3C_2T_x$ plays a crucial role in enabling the electrochemical performance. In addition, the theoretical calculation indicates that the *in-situ* N-doping derived from APTES into the composite also enhances the adsorption of Li ions.

Fig. 1a illustrates the synthesis process of A-$TiO_2/Ti_3C_2T_x$. Initially, $Ti_3C_2T_x$ nanosheets were synthesized according to our recent work [10]. Then, positive APTES was adsorbed onto the negative $Ti_3C_2T_x$ surface *via* electrostatic interactions between them. As confirmed by the zeta potential (Fig. S1 in Supporting information), the potential changes from −23 mV for pure $Ti_3C_2T_x$ to 10 mV after the APTES modification. Along with the hydrolysis of APTES, an ultrathin SiO_2 layer was deposited onto the $Ti_3C_2T_x$ surface, which was further validated by the XRD pattern (Fig. S2 in Supporting information). The broad peak around 23° is ascribed to the SiO_2 characteristic [17]. Moreover, the TEM images also clearly observe the presence of SiO_2 layer (Fig. S3a in Supporting information) compared to pristine $Ti_3C_2T_x$ (Fig. S3b in Supporting information). Subsequently, in a mixed ethanol-glycerol solvent, Ti^{4+} underwent gradual hydrolysis and subsequent hydrothermal treatment, forming a uniform TiO_2 QDs structure onto $Ti_3C_2T_x$ (Fig. S4 in Supporting information). Ultimately, after heat treatment at 600 °C, the A-$TiO_2/Ti_3C_2T_x$ composite with a well-defined morphology is obtained.

Scanning electron microscopy (SEM) and transmission electron microscopy (TEM) technique were used to observe the morphology and structure of A-$TiO_2/Ti_3C_2T_x$. Seen from SEM images (Figs. 1b and c), the composite maintains the lamellar structure of $Ti_3C_2T_x$, and a lot of TiO_2 nanoparticles are uniformly anchored onto the $Ti_3C_2T_x$ surface. The TEM image further confirms the formation of this composite (Fig. 1d). In contrast, the $TiO_2/Ti_3C_2T_x$ sample exhibits a uniform morphology before heat treatment (Fig. S5a in Supporting information). However, after calcination, its whole structure is obviously damaged (Fig. S5b in Supporting information), indicating a poor structural stability. This result indicates that the formed SiO_2 layer serves as a "glue" for tightly coupling the TiO_2 QDs with $Ti_3C_2T_x$. That further enhances the structural stability of A-$TiO_2/Ti_3C_2T_x$, suggesting a superior cycling stability for lithium storage. Figs. 1e and f show the HRTEM images of A-$TiO_2/Ti_3C_2T_x$. Clearly, the TiO_2 nanoparticles are highly dispersed into $Ti_3C_2T_x$. Fig. 1f displays the lattice spacing of 0.352 nm, aligning with the anatase (100) crystal face of TiO_2 [18]. The particle size distribution in Fig. 1g indicates that the TiO_2 QDs size predominantly fell within the range of 1.5–3.5 nm. Additionally, STEM image and energy dispersive spectroscopy (EDS) mapping manifest the uniform distribution of Ti, O, Si, C, and N elements in the composite (Fig. 1h).

Fig. 2a presents the X-ray diffraction (XRD) patterns of two composites. A-$TiO_2/Ti_3C_2T_x$ shows the broad peak around 23°, corresponding to the characteristic peaks of SiO_2 [17], while peaks at 25.3° and 62.7° are assigned to the crystal faces (100) and (204) of anatase TiO_2, indicating the formation of TiO_2 onto the $Ti_3C_2T_x$. Differently, no characteristic peaks of SiO_2 can be observed in $TiO_2/Ti_3C_2T_x$, in accordance with the experimental observations [19]. In Raman spectrum (Fig. 2b), the characteristic peaks at 200 cm^{-1} derived from $Ti_3C_2T_x$ can be visible in three samples. Moreover, the characteristic peaks of TiO_2 at 394, 513 and 635 cm^{-1} are well-indexed in A-$TiO_2/Ti_3C_2T_x$ and $TiO_2/Ti_3C_2T_x$ [12]. Besides, the chemical bonds of two composites were further analyzed *via* FT-IR spectra (Fig. 2c). A-$TiO_2/Ti_3C_2T_x$ and $TiO_2/Ti_3C_2T_x$ both displays the absorption vibration peaks C–F (1097 cm^{-1}) and Ti–O (620 cm^{-1}) belonging to $Ti_3C_2T_x$. However, the absorption vibration peaks of C–N (1050 cm^{-1}) and Si–O (809 cm^{-1}) bonds are observed in A-$TiO_2/Ti_3C_2T_x$ [20], suggesting the existence of SiO_2 originated from the hydrolysis of APTES, which is crucial for the formation of TiO_2 QDs. Additionally, the appearance of C–N (1670 cm^{-1}) and Si–O–Si (459 cm^{-1}) bonds on the $SiO_2/Ti_3C_2T_x$ surface also confirms the point (Fig. S6 in Supporting information) [21]. Based on the N_2 sorption isotherms in Fig. 2d and Fig. S7a (Supporting information), the BET specific surface areas are about 110.1 m^2/g and 100.2 m^2/g for A-$TiO_2/Ti_3C_2T_x$ and $TiO_2/Ti_3C_2T_x$, respectively. The larger surface areas of A-$TiO_2/Ti_3C_2T_x$ can provide the more active sites for lithium storage, suggesting a better performance. Furtherly, two composites both illustrate the mesoporous characteristics (inset of Fig. 2d and Fig. S7b in Supporting information).

X-ray photoelectron spectrometer (XPS) technique was applied to analyze the chemical states of A-$TiO_2/Ti_3C_2T_x$. The survey XPS spectrum confirms the existence of Ti, Si, O, C, and N (Fig. S8a in Supporting information), consistent with the above EDS analysis. And the N atomic content is 1.29% (Fig. S8b in Supporting information), which mainly comes from the containg-NH_2 APTES. Fig. 2e shows the high-resolution spectrum of Ti 2p, the peaks at 459.33 and 465.28 eV are attributed to Ti^{4+}, while the doublet peaks at 456.49 and 464.29 eV are associated with the Ti-C bond. Meanwhile, the Ti-O bond at 459.05 eV is also observed. This further verifies the strong coupling of TiO_2 QDs with $Ti_3C_2T_x$. In the O 1s region, Si–O, Ti–O–C and Ti–O–Ti bonds can be well identified at

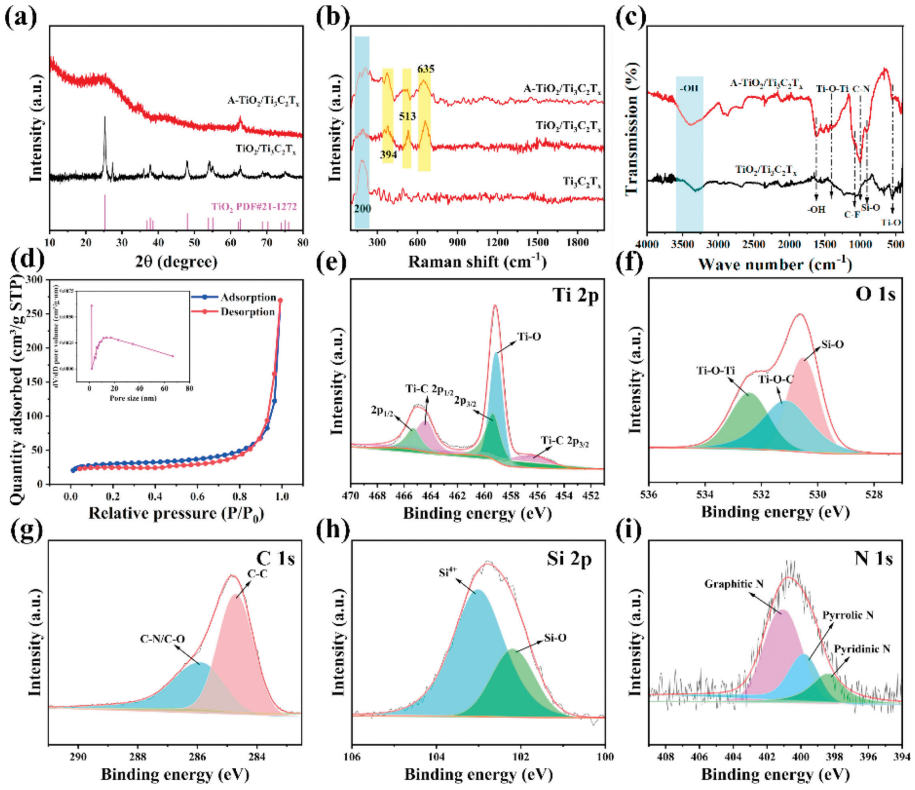

Fig. 2. (a) XRD patterns, (b) Raman spectra, and (c) FT-IR spectra of A-$TiO_2/Ti_3C_2T_x$ and $TiO_2/Ti_3C_2T_x$. (d) N_2 sorption isotherm and corresponding pore size distribution curve, and high-resolution XPS spectra of A-$TiO_2/Ti_3C_2T_x$ for (e) Ti 2p, (f) O 1s, (g) C 1s, (h) Si 2p and (i) N 1s.

the binding energy of 530.5, 531.09 and 532.41 eV (Fig. 2f) [6]. Two peaks at 284.72 eV and 286.08 eV in the C 1s spectrum (Fig. 2g) are ascribed to C–C (284.72 eV) and C-Ti/C–N/C–O [22]. The Si 2p spectrum in Fig. 2h displays distinct Si^{4+} (103 eV) and Si-O (102.19 eV) peaks [21], corresponding to the spectral analysis of O 1s. The N 1s high-resolution spectrum in Fig. 2i shows the presence of pyridinic N (398.3 eV), pyrrolic N (399.8 eV), and graphitic N (401 eV) [23], which can effectively enhance the adsorption of Li ions by heterostructure, thereby promoting the lithium storage capacity of the composite electrode.

To evaluate the lithium storage performance of two composites, a half cell was assembled using lithium metal as the counter electrode. Fig. 3a illustrates the cyclic voltammetry (CV) curves for the first three cycles of the A-$TiO_2/Ti_3C_2T_x$ electrode at a scan rate of 0.1 mV/s. In the first cycle, a cathodic peak appears around 0.75 V, and an anodic peak is observed near 0.95 V, indicating the Li^+ insertion/extraction in the composite [24]. Additionally, an irreversible cathode peak at around 1.75 V and an anode peak at approximately 2.02 V are seen, attributing to the electrochemical activities of TiO_2. The irreversible cathodic peak is related to the formation of a solid electrolyte interface (SEI) [25]. In the following two cycles, the irreversible peaks are significantly reduced, and the curves almost completely overlap. Furthermore, in comparison to $TiO_2/Ti_3C_2T_x$ (Fig. S9a in Supporting information), the CV curve of the A-$TiO_2/Ti_3C_2T_x$ electrode exhibits a more rectangular shape, indicating a superior reversibility during cycling process [26].

The galvanostatic charge/discharge (GDC) curves for the first three cycles of A-$TiO_2/Ti_3C_2T_x$ and $TiO_2/Ti_3C_2T_x$ electrodes are presented in Fig. 3b and Fig. S9b (Supporting information). In the first cycle, the discharge and charge capacities of the A-$TiO_2/Ti_3C_2T_x$ electrode are 820.9 mAh/g and 376.9 mAh/g, respectively, while the $TiO_2/Ti_3C_2T_x$ electrode exhibits a lower initial discharge capacity of only 662.4 mAh/g. Moreover, in subsequent cycles, the A-$TiO_2/Ti_3C_2T_x$ electrode remains a higher capacity, demonstrating an enhanced lithium-storage performance.

The rate performance of two electrodes was shown in Fig. 3c. At the current densities of 0.05, 0.1, 0.2, 0.5, 1.0, and 2.0 A/g, the A-$TiO_2/Ti_3C_2T_x$ electrode delivers the specific capacities of 415.2, 375.8, 348.1, 315.5, 278.9, and 224.3 mAh/g, respectively. Furtherly, when the current density is returned to 0.1 A/g, the capacity increases to 420.4 mAh/g. In contrast, the $TiO_2/Ti_3C_2T_x$ electrode has lower capacities of 370.9, 332.7, 298.3, 213.2, 123.6, and 54.1 mAh/g at the same current densities. Upon returning to 0.1 A/g, only 308 mAh/g of the capacity can be maintained. These results indicate that such a unique heterostructure can promote the lithium ion transport in the electrochemical reaction.

Fig. 3d illustrates the cycle performances of A-$TiO_2/Ti_3C_2T_x$ and $TiO_2/Ti_3C_2T_x$ electrodes at a current density of 0.1 A/g. Clearly, the A-$TiO_2/Ti_3C_2T_x$ electrode has a better cycle performance than that $TiO_2/Ti_3C_2T_x$ electrode. More importantly, it maintains a high specific capacity of 424.7 mAh/g, corresponding to 126% of the theoretical capacity of TiO_2 (335 mAh/g) after 400 cycles. In comparison, the $TiO_2/Ti_3C_2T_x$ electrode only sustains a capacity of 176 mAh/g mAh/g under the same conditions. The outstanding cycling performance of A-$TiO_2/Ti_3C_2T_x$ can be related to its superior structural stability facilitated by the presence of SiO_2 during cycling. Moreover, as listed in Fig. 3e and Table S1 (Supporting information), the newly-developed A-$TiO_2/Ti_3C_2T_x$ electrode in our work is comparable to those TiO_2-based anodes reported [3,27-34].

Impressively, the A-$TiO_2/Ti_3C_2T_x$ anode demonstrates an exceptional long cycling performance. As shown in Fig. 3f, after 2500 cycles, it maintains a specific capacity of 170 mAh/g at a high current density of 1000 mA/g, achieving an average coulombic efficiency of nearly 99.99%. The rate of capacity loss per cycle was a mere 0.009%. In stark contrast, the $TiO_2/Ti_3C_2T_x$ electrode preserves a capacity of only 100 mAh/g after 2500 cycles at the same

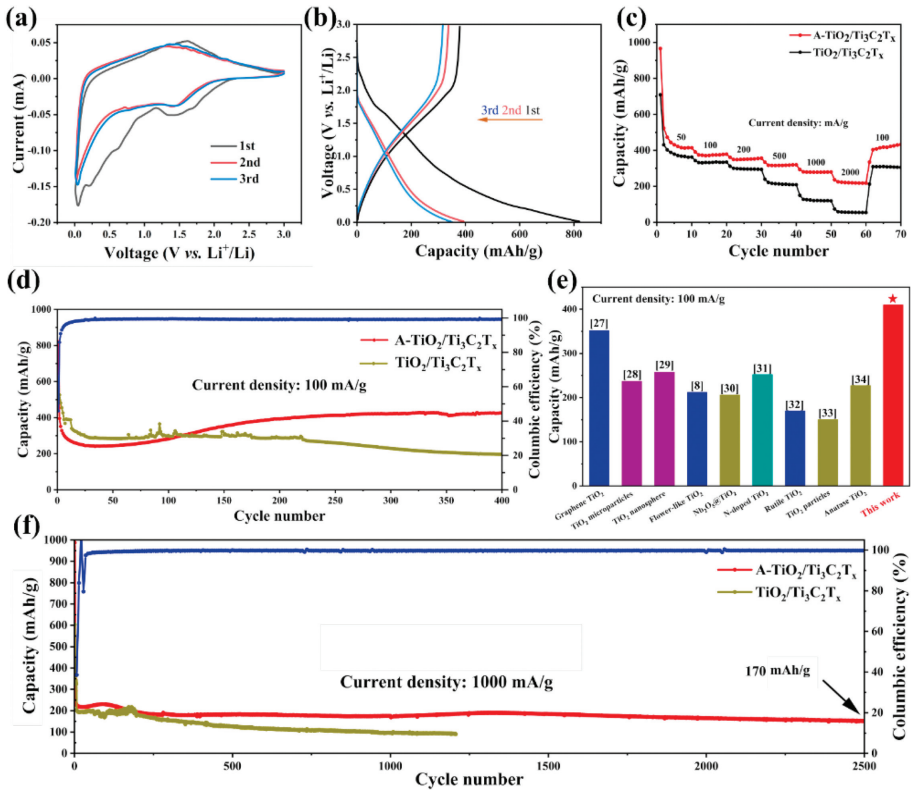

Fig. 3. (a) CV curves of initial three cycles at a scan rate of 0.1 mV/s, and (b) charge-discharge profiles of the A-$TiO_2/Ti_3C_2T_x$ electrode at 100 mA/g. (c) Rate capabilities, (d) cycling performances at 100 mA/g, and (e) comparison of cycle performances between the A-$TiO_2/Ti_3C_2T_x$ electrode and other TiO_2-based anodes for LIBs. (f) Long cycling performances of A-$TiO_2/Ti_3C_2T_x$ and $TiO_2/Ti_3C_2T_x$ electrodes at a high current density of 1000 mA/g.

current density. This contrast underscores the enhanced durability and performance of the A-$TiO_2/Ti_3C_2T_x$ electrode, attributed to the strong coupling effect of TiO_2 QDs and $Ti_3C_2T_x$ nanosheets.

To further demonstrate the N-doping advantages, the contact angles of two electrodes in the electrolytes were tested (Fig. S10 in Supporting information). Obviously, the wettability of the A-$TiO_2/Ti_3C_2T_x$ electrode is superior to that of the $TiO_2/Ti_3C_2T_x$ electrode, suggesting that A-$TiO_2/Ti_3C_2T_x$ has more fully contact with the electrolyte during the electrochemical reaction. This enhanced wettability can be ascribed to the nitrogen introduction. Moreover, the TEM images after cycles of two electrodes (Fig. S11 in Supporting information) further demonstrate that the existence of thin SiO_2 layer in the heterostructure can ensure the stability of A-$TiO_2/Ti_3C_2T_x$ during the long-term cycles, so as to obtain the superior long cycle life.

A series of CV tests were carried out at various scan rates to investigate the transfer behavior of two electrodes. As illustrated in Fig. 4a and Fig. S12a (Supporting information), their curves display comparable profiles and trends. Furthermore, the presence of redox peaks points to rapid electrochemical reactions occurring within the materials. The relationship between the peak current and the scanning rate (ν) determine the material's capacitance and diffusion contributions [35], and the two obey the following relationship:

$$i = a\nu^b \tag{1}$$

$$\log i = b\log\nu + \log a \tag{2}$$

where a and b are constants, and the fitted value of b (Eq. 2) can indicate whether the electrode dynamic process is primarily governed by capacitance control (b~1.0) or diffusion control (b~0.5) [36]. In Fig. 4b, the fitting b values for the cathode and anode peaks of A-$TiO_2/Ti_3C_2T_x$ are 0.90 and 0.84, respectively, suggesting a capacitance-controlled electrochemical process. Conversely, for $TiO_2/Ti_3C_2T_x$ electrode, the fitted b values for the cathode and anode peaks are 0.61 and 0.56, respectively, indicating a diffusion-dominated behavior (Fig. S12b in Supporting information). The contribution of capacitance and diffusion control to capacity is analyzed by using the following formula [37]:

$$i(\nu) = k_1\nu + k_2\nu^{1/2} \tag{3}$$

where $k_1\nu$ and $k_2\nu$ represent non-Faraday reactions and Faraday reactions, respectively. As depicted in Fig. 4c and Fig. S13a (Supporting information), at a scan rate of 1.0 mV/s, the capacitance contribution ratio is found to be 74.8% for A-$TiO_2/Ti_3C_2T_x$ and 66.2% for $TiO_2/Ti_3C_2T_x$, respectively. Moreover, the capacitance contribution values were computed for multiple sweep speeds simultaneously. As illustrated in Fig. 4d and Fig. S13b (Supporting information), the A-$TiO_2/Ti_3C_2T_x$ electrode exhibits a higher capacitance contribution rate across all scanning rates than $TiO_2/Ti_3C_2T_x$. That indicates its better transport dynamics, thereby improving the rate performance of A-$TiO_2/Ti_3C_2T_x$.

Fig. 4e presents the galvanostatic intermittent titration technique (GITT) curves of A-$TiO_2/Ti_3C_2T_x$ and $TiO_2/Ti_3C_2T_x$ electrodes. The Li^+ diffusion coefficients of two electrodes were calculated based on Fick's second law and the following equation [38]:

$$D = \frac{4}{\pi\tau}\left(\frac{m_B V_m}{M_B S}\right)^2\left(\frac{\Delta E_s}{\Delta E_\tau}\right) \tag{4}$$

As shown in Fig. 4f, the D_{Li^+} values of two electrodes are relatively similar [39]. However, the overall D_{Li^+} levels of the A-$TiO_2/Ti_3C_2T_x$ electrode is higher than those of $TiO_2/Ti_3C_2T_x$. These results further confirm that the A-$TiO_2/Ti_3C_2T_x$ electrode exhibits an enhanced Li^+ diffusion ability, thus effectively improving the energy storage performance.

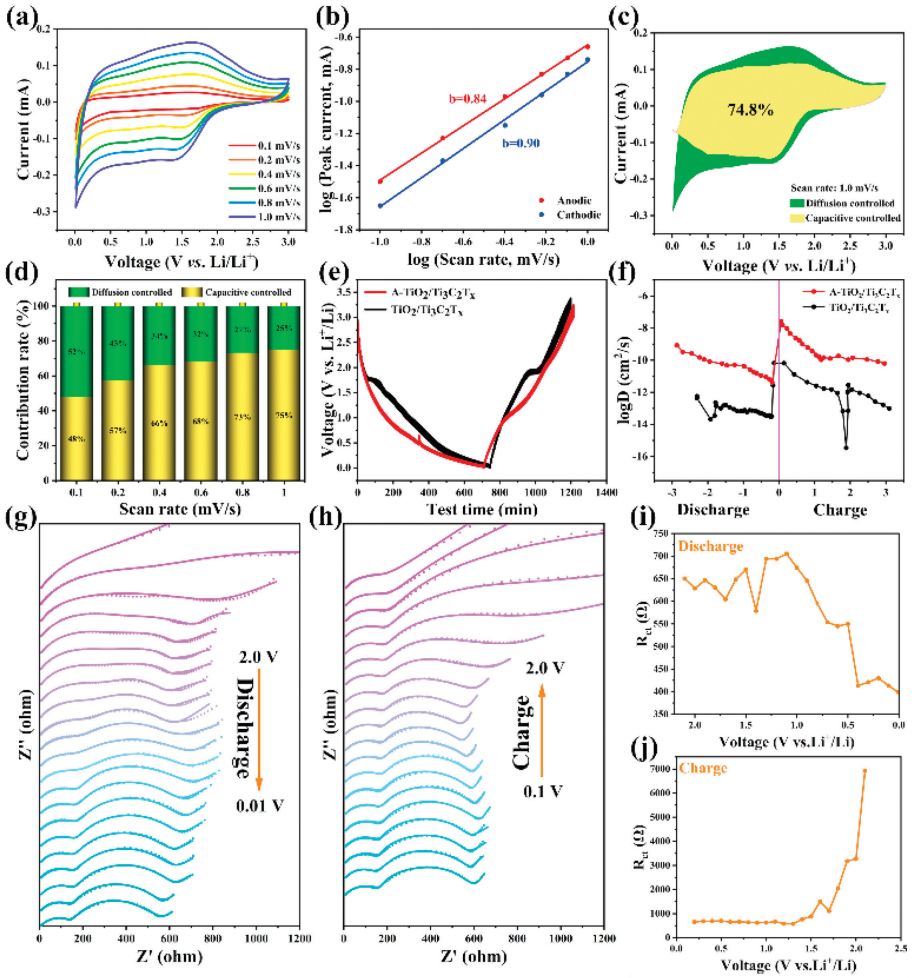

Fig. 4. (a) CV curves at various scan rates, (b) the calculated *b* values at six redox peaks, (c) surface capacitive contribution at 1.0 mV/s, and (d) the percentage of capacitive contribution of the A-$TiO_2/Ti_3C_2T_x$ electrode at diverse scan rates. (e) GITT curves of A-$TiO_2/Ti_3C_2T_x$ and $TiO_2/Ti_3C_2T_x$ electrodes and their (f) Li^+ diffusion coefficients. *In-situ* EIS diagram of (g) discharge and (h) charge of A-$TiO_2/Ti_3C_2T_x$, and calculated R_{ct} resistance values for (i) discharge and (j) charge.

In-situ electrochemical impedance spectroscopy (EIS) was also conducted to analysis the impedance changes of A-$TiO_2/Ti_3C_2T_x$ electrodes during the first cycle. The data was fitted with a suitable circuit, yielding the 2D Nyquist diagram, as depicted in Figs. 4g and h (where the line graph represents the fitted data). With the discharge to 1.7–1.0 V, the SEI film gradually forms, Nyquist curve in the intermediate frequency region is semicircular, indicating the resistance value of the SEI film [40]. The semicircle of the R_{ct} resistance region at this point also tends to stabilize (Fig. 4g). In the final process, two semicircular resistors are stabilized as R_{SEI} and R_{ct}, indicating the complete formation of the SEI film. In the subsequent charging process (Fig. 4h), the R_{SEI} resistance tends to stabilize, and only the R_{ct} resistance region gradually increases until it appears as a straight line. This change indicates the formation of the stable SEI film on the material's surface [41]. Additionally, based on the fitting results, the changes in R_{ct} during the charge and discharge processes were plotted (Figs. 4i and j), in line with the changes observed in the Nyquist curve and confirmed the above changes in R_{ct}.

Then, we calculate the adsorption energy and surface charge density difference to show the enhancement of the Li adsorption and surface electron redistribution in the $TiO_2/Ti_3C_2N_2$ heterostructure compared to TiO_2/Ti_3C_2, $Ti_3C_2N_2$ and TiO_2 surface. Two adsorption sites at the TiO_2 (I for Ti-top and II for O-top) and Ti_3C_2 surface (I for C-hollow, II for Ti-hollow) were choose, respectively, to identity the more stable one for Li adsorption. As presented in Fig. 5a, the Li adsorption energy on the $TiO_2/Ti_3C_2N_2$ reaches −6.73 eV at the C-hollow site (I), significantly lower than those on TiO_2/Ti_3C_2 (−1.06 eV), $Ti_3C_2N_2$ (−4.04 eV) and TiO_2 surface (−3.21 eV), manifesting the enhanced Li adsorption stability in the $TiO_2/Ti_3C_2N_2$. Besides, the charge density difference shows that the electrons preferred to deplete from the Li-ion and accumulate at the surface of the substrate, suggesting the electron transfer from the Li to the Ti_3C_2 or TiO_2 surface. The Bader analysis exhibits the 0.38e, 0.07e, 0.35e and 0.26e electrons transfer from the Li to the $TiO_2/Ti_3C_2N_2$, TiO_2/Ti_3C_2, $Ti_3C_2N_2$ and TiO_2 surface, respectively (Fig. 5b). Herein, the $TiO_2/Ti_3C_2N_2$ heterostructure attracts more electrons from the Li-ion, rendering it a stronger interaction on Li adsorption. Therefore, the enhanced adsorption of Li ions makes the $TiO_2/Ti_3C_2N_2$ heterostructure a promising electrode material for LIBs.

Based on the above results, the outstanding lithium storage performance of the A-$TiO_2/Ti_3C_2T_x$ electrode is mainly due to the following reasons (Fig. 5c): Firstly, the construction of 0D/2D heterostructure shortens the ion transport path, thus promoting the rapid transfer dynamics during cycles. Secondly, $Ti_3C_2T_x$ nanosheets as the substrate establishes an excellent conductive network, effectively enhancing the conductivity of the whole electrode, and ultrasmall TiO_2 QDs provide the exposure of more active sites for lithium-ion storage, thereby boosting the reversible capacity. Furthermore, the N atoms derived from APTES enhance the adsorption of lithium ions, leading to increased lithium storage. More

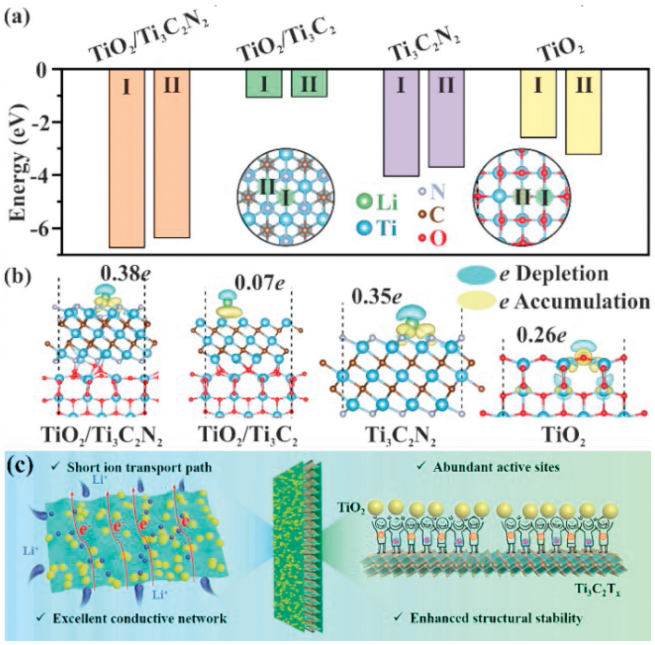

Fig. 5. (a) Lithium adsorption energies (E_{ads}) at different sites (I and II) for $TiO_2/Ti_3C_2N_2$, TiO_2/Ti_3C_2, $Ti_3C_2N_2$ and TiO_2 surface, respectively. (b) Corresponding charge density difference (iso-value of 0.002 e/Å^3) for each surface at their most stable site. (c) Schematic diagram of lithium storage merits of A-$TiO_2/Ti_3C_2T_x$.

importantly, the SiO_2 layer ensures the tight attachment of TiO_2 QDs onto the $Ti_3C_2T_x$ surface, significantly enhancing the structural integrity of the overall composite during the long cycling.

In summary, a new type of 0D TiO_2 quantum dots/2D $Ti_3C_2T_x$ composite with exceptional lithium storage performance has been constructed using the APTES-induced assembly route. The results indicate that the SiO_2 layer formed from the APTES hydrolysis significantly improves the structural stability of the whole electrode. The prepared A-$TiO_2/Ti_3C_2T_x$ anode maintains a high capacity of 425.4 mAh/g after 400 cycles at 100 mA/g, surpassing the theoretical capacity of original TiO_2 by 126%. Furthermore, it has an impressive long-cycling performance, retaining a capacity of 170 mAh/g after 2500 cycles at 1000 mA/g. Through electrochemical kinetics analysis combining with DFT calculation, the excellent lithium storage performance of A-$TiO_2/Ti_3C_2T_x$ is attributed to its unique heterostructure and *in-situ* N doping derived from APTES, which not only reduces the Li^+ adsorption energy, but also gives the fast charge transfer dynamics. The strategy proposed in our work offers a promising approach towards high-performance nanocomposites with enhanced structural stability.

Declaration of competing interest

The authors declare that they have no known competing financial interests or personal relationships that could have appeared to influence the work reported in this paper.

CRediT authorship contribution statement

Xinlin Zhang: Investigation, Methodology, Writing – original draft. **Cheng Tang:** Software. **Haitao Li:** Validation. **Jie Sun:** Data curation. **Aijun Du:** Validation. **Minghong Wu:** Funding acquisition. **Haijiao Zhang:** Conceptualization, Project administration, Supervision, Writing – review & editing.

Acknowledgments

We appreciate the support from the Natural Science Foundation of Shanghai (No. 23ZR1423800), and Key Laboratory of Advanced Energy Materials Chemistry (Ministry of Education), Nankai University.

Supplementary materials

Supplementary material associated with this article can be found, in the online version, at doi:10.1016/j.cclet.2024.110088.

References

[1] X. Xiao, Z.J. Zhang, W.T. Yu, et al., Appl. Energy 328 (2022) 120186.
[2] F.Y. He, C. Tang, Y.D. Liu, et al., J. Mater. Sci. Technol. 100 (2022) 101–109.
[3] L. Luo, K. Liang, Z. Khanam, et al., Small 20 (2024) 2307103.
[4] C.F. Zhang, M. Beidaghi, M. Naguib, et al., Chem. Mater. 28 (2016) 3937–3943.
[5] J. Jang, H.s. Kim, S. Moon, et al., Nano Lett. 22 (2022) 761–767.
[6] M.H. Wu, L.B. Gu, Q. Wang, et al., ChemNanoMat 4 (2018) 387–393.
[7] C.F. Zhang, S.J. Kim, M. Ghidiu, et al., Adv. Funct. Mater. 26 (2016) 4143–4151.
[8] I.Z. Nejad, N. Zolfaghari, M.M. Mashhadi, et al., Sustain. Energy Technol. Assess. 47 (2021) 101438.
[9] W.L. Cai, C. Yan, Y.X. Yao, et al., Small Struct. 1 (2020) 2000010.
[10] H.T. Li, F.T. Lv, X. Fang, et al., Carbon Neutral. 2 (2023) 678–688.
[11] Y.P. Wang, P.C. Yuan, Z.Y. Xu, et al., Chin. Chem. Lett. 35 (2024) 108776.
[12] H.A. Tariq, U. Nisar, J.J. Abraham, et al., Appl. Surf. Sci. 583 (2022) 152441.
[13] L. Li, G.X. Jiang, C.H. An, et al., Nanoscale 12 (2020) 10369–10379.
[14] M.H. Wu, Y.P. Gao, Y. Hu, et al., Chin. Chem. Lett. 31 (2020) 897–902.
[15] H. Zhang, L. Yang, P.G. Zhang, et al., Adv. Mater. 33 (2021) 2008447.
[16] L. Petrizza, D. Genovese, G. Valenti, et al., Electroanalysis 28 (2016) 2777–2784.
[17] X.L. Liu, Y.X. Chen, H.B. Liu, et al., J. Mater. Sci. Technol. 33 (2017) 239–245.
[18] Y. Zhang, Z.H. Bao, R. Wang, et al., Nanoscale 16 (2024) 1751–1757.
[19] J.P. Yang, Y.X. Wang, W. Li, et al., Adv. Mater. 29 (2017) 1700523.
[20] N. Talreja, M. Ashfaq, D. Chauhan, et al., Mater. Chem. Phys. 294 (2023) 127029.
[21] Q. Liu, Y.X. Ji, X.M. Yin, et al., Energy Storage Mater. 46 (2022) 384–393.
[22] Y.C. Zhang, Y. Tian, Z.R. Wang, et al., Chem. Eng. J. 458 (2023) 141388.
[23] N. Huang, C. Tang, H. Jiang, et al., Nano Res. 17 (2023) 2619–2627.
[24] C. Yang, Y. Liu, X. Sun, et al., Electrochim. Acta 271 (2018) 165–172.
[25] X.F. Lou, Y.Y. Zhang, L. Zhao, et al., Sci. Rep. 13 (2023) 18560.
[26] Y. Li, S. Wang, D.N. Lei, et al., J. Mater. Chem. A 5 (2017) 12236–12242.
[27] H.L. Wang, P.C. Zhang, P.F. Huang, J. Chem. Technol. Biotechnol. 97 (2022) 2815–2819.
[28] W. Devina, D. Nam, J. Hwang, et al., Electrochim. Acta 321 (2019) 134639.
[29] Y.J. Zheng, B.J. Liu, P. Cao, et al., J. Mater. Sci. Technol. 35 (2019) 667–673.
[30] W.L. Xu, Y.L. Xu, T. Schultz, et al., ACS Appl. Mater. Interfaces 15 (2022) 795–805.
[31] G. Hasegawa, T. Sato, K. Kanamori, et al., New J. Chem. 38 (2014) 1380–1384.
[32] D. McNulty, E. Carroll, C. O'Dwyer, Adv. Energy Mater. 7 (2017) 1602291.
[33] M.N. Hyder, B.M. Gallant, N.J. Shah, et al., Nano Lett. 13 (2013) 4610–4619.
[34] M.N. Tahir, B. Oschmann, D. Buchholz, et al., Adv. Energy Mater. 6 (2016) 1501489.
[35] F.Y. He, C. Tang, G.J. Zhu, et al., Sci. China Chem. 64 (2021) 964–973.
[36] D.P. Li, X.H. Ren, Q. Ai, et al., Adv. Energy Mater. 8 (2018) 1802386.
[37] W.X. Zhao, X.Q. Ma, X.D. Wang, et al., J. Mater. Chem. A 11 (2023) 2431–2442.
[38] L.B. Tang, P.Y. Li, R.D. Cui, et al., Small Methods 7 (2023) 2201387.
[39] S.F. Ho, H.Y. Tuan, Chem. Eng. J. 452 (2023) 139199.
[40] D.G. Sun, C. Tang, H. Cheng, et al., J. Energy Chem. 72 (2022) 479–486.
[41] M.M. Abdelaal, C.C. Yang, T.F. Hung, J. Energy Storage 77 (2024) 109926.